



UvA-DARE (Digital Academic Repository)

Glow with the flow: Quantifying blood flow and photoluminescence signal in biological tissue

Nadort, A.

Publication date

2015

Document Version

Final published version

[Link to publication](#)

Citation for published version (APA):

Nadort, A. (2015). *Glow with the flow: Quantifying blood flow and photoluminescence signal in biological tissue*. [Thesis, fully internal, Universiteit van Amsterdam].

General rights

It is not permitted to download or to forward/distribute the text or part of it without the consent of the author(s) and/or copyright holder(s), other than for strictly personal, individual use, unless the work is under an open content license (like Creative Commons).

Disclaimer/Complaints regulations

If you believe that digital publication of certain material infringes any of your rights or (privacy) interests, please let the Library know, stating your reasons. In case of a legitimate complaint, the Library will make the material inaccessible and/or remove it from the website. Please Ask the Library: <https://uba.uva.nl/en/contact>, or a letter to: Library of the University of Amsterdam, Secretariat, P.O. Box 19185, 1000 GD Amsterdam, The Netherlands. You will be contacted as soon as possible.



7

FEASIBILITY STUDY OF THE OPTICAL IMAGING OF A
BREAST CANCER LESION LABELED WITH UPCONVERSION
NANOPARTICLE BIOCOMPLEXES

Adapted from:

E. A. Grebenik, **A. Nadort**, A. N. Generalova, A. V. Nechaev, V. K. Sreenivasan, E. V. Khaydukov, V. A. Semchishen, A. P. Popov, V. I. Sokolov, and A. S. Akhmanov, "Feasibility study of the optical imaging of a breast cancer lesion labeled with upconversion nanoparticle biocomplexes," *J. Biomed. Opt.* 18, 076004-076004 (2013).

7

ABSTRACT Innovative luminescent nanomaterials, termed upconversion nanoparticles (UCNPs), have demonstrated considerable promise as molecular probes for high-contrast optical imaging in cells and small animals. The feasibility study of optical diagnostics in humans is reported here based on experimental and theoretical modelling of optical imaging of an UCNP-labelled breast cancer lesion. UCNPs synthesized in-house were surface-capped with an amphiphilic polymer to achieve good colloidal stability in aqueous buffer solutions. The scFv4D5 mini-antibodies were grafted onto the UCNPs via a high-affinity molecular linker barstar:barnase (Bs:Bn) to allow their specific binding to the human epidermal growth factor receptor HER2/neu, which is overexpressed in human breast adenocarcinoma cells SK-BR-3. UCNP-Bs:Bn-scFv4D5 biocomplexes exhibited high-specific immobilization on the SK-BR-3 cells with the optical contrast as high as 10:1 benchmarked against a negative control cell line. Breast cancer optical diagnostics was experimentally modelled by means of epi-luminescence imaging of a monolayer of the UCNP-labelled SK-BR-3 cells buried under a breast tissue mimicking optical phantom. The experimental results were analysed theoretically and projected to in vivo detection of early-stage breast cancer. The model predicts that the UCNP-assisted cancer detection is feasible up to 4 mm in tissue depth, showing considerable potential for diagnostic and image-guided surgery applications.

7.1 INTRODUCTION

Discrimination between healthy and pathological tissue is at the heart of medical diagnostics, where optical imaging can offer non-invasive affordable solutions for accessible organs, such as the skin and hollow organs [1,2]. For example, diffuse optical tomography localizes a pathological lesion through the altered light scattering and absorption properties resulting from abnormal physiological conditions (manifested through e.g. blood oxygenation, bilirubin concentration, etc.), achievable in the centimetre-range surface depths [1]. This is a non-invasive and patient friendly technique. However, the poor spatial resolution and non-specificity represent shortfalls of this technique [3].

Labelling pathological lesions with molecular probes overcomes these shortfalls by enhancing the molecular contrast, as has been recently demonstrated in a number of studies [4,5]. Such a molecular probe comprises two functional modules: a targeting vector and a contrast agent. The targeting vector's functionality requires high affinity and specificity for the targeted tissue site, such as cell receptors in the case of a cancerous lesion, and often employs peptide ligands or antibodies [3]. One of the accepted targets for cancer diagnostics is the human epidermal growth factor receptor 2 (HER2/neu), which is overexpressed in a number of cancers and often accompanied by high drug resistance [6]. Identification and precise localization of a cancerous lesion using minimally invasive optical means, can aid diagnostic and therapeutic decisions. A recombinant scFv4D5 mini-antibody is an example of a high-efficiency HER2/neu-targeting vector that represents a single chain variable fragment of immunoglobulin (Ig) and exhibits lower cross-reactivity and immunogenicity in comparison with the corresponding full-size antibody [7].

The use of contrast agents, exploiting their fluorescent or, more generally, luminescent properties, is widespread in biomedical optical imaging. These luminescent molecular probes allow high-sensitivity and high-resolution imaging, since the absorbed excitation light is re-emitted as luminescence in a different spectral band, which can be spectrally discriminated from the excitation light. Despite a number of successful applications of these molecular probes in many areas of the life sciences, several challenges limit their application scope in e.g. *in vivo* biomedical optical imaging. First, the vast majority of luminescent molecular probes is excited by light in the ultraviolet (UV) or visible spectral ranges, while the emitted luminescence signal is detectable in the visible spectral range, where both excitation and emission light are strongly absorbed and scattered by biological tissues. Second, the exposure of live biological tissue to light in this spectral range induces intrinsic fluorescence, termed autofluorescence, due to its constituent endogenous (intrinsic) fluorophores. Both the luminescence of the exogenous (extraneously introduced) molecular probes and biotissue autofluorescence are shifted to longer wavelength (Stokes shift). Although signals generated by the luminescent molecular probe and the autofluorescence background are separable using spectral methods, the practical efficiency of these approaches is limited [8]. Several other shortfalls that impede the widespread implementation of luminescent agents include toxic effects (quantum dots) and poor thermal and photochemical stability (green fluorescent protein, red fluorescent protein, luciferase-mediated bioluminescence) [9,10]. Moreover, long-term excitation radiation of the luminescent probes in UV or visible spectral ranges can cause tissue photodamage [9].

A recent breakthrough in synthetic chemistry has resulted in a highly efficient luminescent nanomaterial termed upconversion nanoparticles (UCNPs) [11]. The most popular type of UCNPs is an NaYF_4 nanocrystal codoped with ytterbium (Yb^{3+}) and erbium (Er^{3+}) lanthanide ions (short-hand notation, $\text{NaYF}_4:\text{Yb,Er}$) [12]. The absorbed photon energy conversion in UCNPs occurs through complex multistage processes that include conversion of two or more near infrared (NIR) excitation photons (typically, at wavelength 980 nm) to higher energy emission in the visible and NIR spectral range, as detailed previously in Chapters 5 and 6. To recall, the main advantages of the UCNPs in the context of optical biomedical imaging applications are as follows. The spectral bands of the excitation light (980 nm) and part of the emitted luminescence response, fall into the so-called biological tissue “transparency window” (650 to 1300 nm), where light penetration in tissue takes place with minimal absorption and scattering. The autofluorescence response of live biological tissue at this excitation wavelength is insignificant and very often undetectable. Furthermore, UCNP emission is spectrally shifted toward shorter wavelength (anti-Stokes shift), making spectral separation of the luminescence and autofluorescence signals easy and efficient [13]. Moreover, the exceptionally long luminescence lifetime of UCNPs (sub-milliseconds), enables the implementation of an optical time-gated scheme that is capable of completely suppressing the short-lifetime autofluorescence background and scattered excitation light [14].

The promise of UCNPs has recently been demonstrated by imaging UCNP-based biocomplexes in cell cultures and small animal models, which showed that the autofluorescence background was suppressed [15–19]. For example, Zhan et al. have demonstrated labeling a HeLa cancer cell line with noncovalent conjugates of UCNP and anti-carcinoembryonic antigen (CEA)8 antibody followed by *in vitro* cell imaging. The anti-CEA8 is commonly used to immunologically detect the CEA, a cancer biomarker expressed on the surface of HeLa cells [18]. *In vivo* optical imaging of U87MG human glioblastoma tumors in living nude mice was reported by Xiong et al., where an arginine–glycine–aspartic peptide served as the targeting vector capable of specifically bind to $\alpha\text{v}\beta3$ integrin receptor overexpressed in the case of tumour angiogenesis [17].

However, the feasibility of optical imaging in live human tissue assisted by UCNP-based molecular probes under the biologically safe laser excitation conditions remains largely unexplored. The evaluation of the possibility of UCNP-assisted optical imaging in the context of early-stage cancer diagnostics is the key goal of this study. To this end, we report on UCNP synthesis and characterization in-house, followed by surface polymer coating which stabilizes the particles in aqueous buffer colloids. A flexible modular design using a high-affinity molecular linker barstar:barnase (Bs:Bn) was instrumental to achieve bioconjugation of the UCNP to the targeting vector, resulting the assembly of UCNP-scFv4D5 mini-antibody biocomplexes [6,20]. Human breast adenocarcinoma cells SK-BR-3 overexpressing HER2/ neu were target-labelled with the UCNP biocomplexes and imaged using epi-luminescence microscopy. Optical imaging of a compact cancer cell cluster (pertinent to cancer stage I) was simulated using our breast cancer cell model covered with an optical phantom that reproduced breast tissue properties. The experimental imaging data enabled the theoretical evaluation of the feasibility of UCNP-assisted optical diagnostic imaging of a cancerous site in human breast tissue.

The key advance of our work is quantitative modelling of the optical imaging of early-stage breast cancer, where all integral parts of our model, including nanoparticle specific immobilization on the cancer cells, optical tissue phantom and optical imaging system, are well-controlled and characterized. This allows realistic evaluation of the feasibility of the optical imaging of an UCNP-labelled cancer lesion *in vivo*, albeit not in clinical, but in laboratory settings.

7.2 MATERIALS AND METHODS

7.2.1 Synthesis of β -NaY_{0.78}Yb_{0.2}Er_{0.02}F₄ UCNPs

All chemicals were purchased from Sigma–Aldrich (Germany). Nanoparticles of programmable size and crystal phase were grown from a solution of sodium metal salts and oleic acid in an oxygen-free atmosphere at elevated temperatures. The mixture of Y₂O₃ (0.78 mmol), Yb₂O₃ (0.2 mmol), and Er₂O₃ (0.02 mmol) was refluxed in 70% trifluoroacetic acid (20 ml) for ca. 6 h. The resulting clear solution was cooled to room temperature and the solvent was evaporated. The obtained residue was dried under vacuum at 0.1 torr for 3 h and thoroughly ground in an agate mortar until a fine homogeneous powder was produced. This powder was mixed with sodium trifluoroacetate (2 mmol), oleic acid (6 ml), and 1-octadecene (6 ml) in a three-necked flask equipped with a thermometer and magnetic stirrer, and stirred at 100°C under vacuum for 30 min. The degassed and water-free mixture was gradually heated to 290°C at a rate of 6 °C/min and kept at this temperature for 45 min under an argon atmosphere. The temperature was then raised to 310°C for 70 min. Next, the solution was cooled, suspended in propanol-2 (130 ml), and centrifuged at 6000 rpm for 30 min (Z206A centrifuge, Hermle, Germany). The as-synthesized particles were washed with absolute ethanol four times and dried. The particles were then dissolved in chloroform (10 ml), precipitated with propanol-2 (50 ml), and centrifuged at 4000 rpm for twice 10 min. The final product was dried at room temperature [11].

7.2.2 Protein Production and Characterization

We isolated and purified the Bn-scFv4D5 fusion protein, as described by Deyev et al. [20] with slight modifications. *Escherichia coli* strain SB536 [F⁻, WG1, Δ*fhuA* (ton Δ), Δ*hhoAB* (SacII), *shh*] was transformed with the pSD4D5BnHis5 plasmid with the inserted Bs-coding moiety protecting bacterial cells from Bn cytotoxic effect. The transformants were then grown in YTPS broth (1% yeast extract, 1% trypton, 150 mM NaCl, 40 mM K₂HPO₄, 10 mM KH₂PO₄, 2 mM MgCl₂, 0.1 g/l ampicillin, pH 7.5) at 37°C until the optical density at 560 nm wavelength (OD₅₆₀) reached 0.6, and supplied with isopropyl β-D-1-thiogalactopyranoside (1 mM) for 5-h *lac* promoter induction. The obtained biomass was harvested by centrifugation (Allegra 21R Centrifuge, Beckman Coulter, USA) and disintegrated on ice by sonication in a lysis buffer [5 mM tris(hydroxymethyl)aminomethane–hydrochloride (Tris–HCl), 40 mM K₂HPO₄, 500 mM NaCl, pH 8.2]. The extract was clarified by centrifugation and filtration through a membrane filter (220-nm pore size) and loaded onto a HiTrap nickel-nitrilotriacetic acid 1-ml column (GE Healthcare Worldwide). In order to remove the Bs inhibitor, the column was washed with urea solution (8 M), with subsequent refolding of the fusion protein by a linear urea concentration gradient (8–0 M). The refolded protein was then eluted by a 225-mM imidazole solution and transferred to a phosphate buffer (20 mM NaCl, 6.5 mM NaH₂PO₄, 41 mM Na₂HPO₄, pH 6.5) using

a PD-10 desalting column (GE Healthcare Worldwide), and finally purified in a HiTrap SP-Sepharose Fast Flow 1-ml column (GE Healthcare Worldwide). Electrophoretic analysis of eluted fractions in polyacrylamide gel (12.5%) showed the Bn-scFv4D5 elution at 275 mM NaCl.

The Bs C40A protein was produced using *E. coli* strain HB101 [$F^- \Delta(gpt-proA)62 leu B6 glnV44 ara-14 galK2 lacY1 \Delta(mcrC-mrr) rpsL20 (Str^r) xyl-5 mtl-1recA13$], carrying pMT641 plasmid [6]. The cells were cultivated in YTPS broth until the stationary growth phase, and then centrifuged, followed by re-suspension in cold lysis buffer [0.05 M Tris-HCl, 0.1 M NaCl, 10 mM ethylenediaminetetraacetic acid (EDTA), 10 mM dithiothreitol (DTT), pH 8.0]. The obtained solution was sonicated on ice with a 30% ammonium sulfate saturation for cell disruption followed by nucleic acid precipitation with poly (ethyleneimine). Further, the cell extract was clarified by centrifugation and Bs content was precipitated by 70% ammonium sulfate saturation. The resulting precipitate was dissolved in TD buffer (0.1 M Tris-HCl, 10 mM EDTA, 10 mM DTT, pH 8.0) and fractionated according to protein size in a Sephadex G-100 SuperFine column (C16/100) equilibrated with TSDT buffer (0.02 M Tris-HCl, 0.02 M NaCl, 2 mM EDTA, 2 mM DTT, 0.05% Tween-20, pH 8.0). Finally, Bs was purified in a HiTrap Q-Sepharose Fast Flow 1-ml column (GE Healthcare Worldwide) equilibrated with TDG buffer (0.2 M Tris-HCl, 2 mM DTT, 10% glycerol, pH 8.0). Elution was performed with a NaCl concentration gradient. The Bs was identified by polyacrylamide gel (17%) electrophoresis.

Ribonucleic activity of the recombinant protein, BnscFv4D5 was determined by the acid-insoluble ribonucleic acid (RNA) precipitation assay [21]. 40- μ l dilutions (from 30 to 0.015 nM) of the analysed protein in Tris-HCl buffer (0.125 M Tris-HCl, pH 8.5) were mixed with 160 μ l yeast RNA aliquots (2 mg/ml) and allowed enzymatic RNA splitting at 37°C. After 15 min, the reaction was stopped by adding 6% chloric acid (200 μ l) to the mixture at +2°C for 15 min. Non-reacted RNA substrate was removed by centrifugation (Eppendorf 5415D Centrifuge, Germany) and supernatants were analysed for released nucleotide concentrations, which determine the OD₂₆₀. To estimate the Bs:Bn affinity, different Bs dilutions were added to a solution of Bn at a constant saturation concentration followed by the same measurements. In the last case, Bs concentration was inversely proportional to the OD₂₆₀.

ScFv4D5-HER2/neu affinity was evaluated by using antihuman polyclonal antibodies. A 96-well flat-bottomed polystyrene plate was coated with a recombinant p185^{HER2-EDC} antigen prepared in coating buffer (0.1 M Na₂CO₃, 0.1 M NaHCO₃, pH 9.2) at amounts of 8 and 16 ng/well. After 1 h antigen absorption, the plate was washed with phosphate-buffered saline (PBS) and unsaturated surface-binding sites were blocked with a blocking solution [5% milk (Tesco, UK) in PBS, pH 7.4]. The Bn-scFv4D5 solved in PBS with Tween-20 (0.1%) was then added at different dilutions with a starting concentration of 5 nM. After 1 h of incubation with constant shaking in a rocker shaker, the plate was washed. To detect the immobilized Bn-scFv4D5, first, polyclonal rabbit-anti-human antibody and second, peroxidase-conjugated goat-anti-rabbit IgG were used with washing between the steps. For subsequent colourimetric measurement 1,2-diaminobenzene (Sigma-Aldrich, Germany) (0.04%) with hydrogen peroxide (0.06%) in citric buffer (7.3 g/l citric acid, 11.86 g/l Na₂HPO₄·2H₂O, pH 5) were added to the wells. The reaction was stopped by

adding 2 M sulfuric acid (50 μ l). The OD₄₅₀ was read using a plate spectrophotometer (StatFax-2100, Awareness Technology, USA). The affinity constant (K_{off}) was calculated, as described by Beatty et al. [22] with consideration of antibody monovalency using the following equation:

$$K_{\text{off}} = \frac{(n-1)}{n[Ab']_f - [Ab]_f} \quad (7.1)$$

where $[Ab']_f$ and $[Ab]_f$ are the total antibody concentrations, in the wells at OD-50' and OD-50 for plates coated with total antigen concentrations of $[Ag']_f$ (8 ng) and $[Ag]_f$ (16 ng), respectively, and

$$n = \frac{[Ag]_f}{[Ag']_f} \quad (7.2)$$

7.2.3 Bioconjugation of UCNPs

The as-synthesized UCNPs were coated with poly(maleic anhydride-*alt*-1-octadecene) amphiphilic polymer [PMAO (Sigma–Aldrich, Germany)], as described by Pellegrino et al. [23] with slight modifications. 1,6-Diaminohexane (Serva, Germany) was added to cross-link the PMAO chains around the particles. In order to link the biomolecules to the UCNPs, the surface carboxylic groups of the PMAO shell were activated in a cold buffered aqueous solution with an excess of 1-ethyl-3-(3-dimethylaminopropyl)carbodiimide (EDC) and N-hydroxysulfosuccinimide (sulfo-NHS) cross-linkers (Sigma–Aldrich, Germany) under sonication. The nanoparticles were then washed from unreacted cross-linkers by centrifugation at 4°C, re-dispersed in cold Bs solution, and allowed to bind to Bs overnight. The unbound Bs molecules were removed from the solution by three centrifugation–re-suspension cycles, and the resultant product was stored in PBS.

7.2.4 Transmission Electron Microscopy (TEM)

The UCNP and PMAO–UCNP solutions were diluted by *n*-hexane and water, respectively, then sonicated and dropcasted onto a thin bar 300-mesh copper TEM grids, coated with 0.3% pioloform. After overnight drying in a desiccator at room temperature, the grids were imaged using a Philips CM10 TEM (Philips, Eindhoven, The Netherlands). ImageJ freeware was used for UCNP size distribution analysis.

7.2.5 Fourier Transform Infrared (FTIR) Spectroscopy

Pure PMAO was thoroughly ground and then pressed with KBr to form a tablet. The UCNP modified with PMAO was dried using a Savant SpeedVac Concentrator (France), then ground and pressed with KBr to form a tablet. FTIR spectra were recorded using an FTIR spectrophotometer (Varian 3100, USA).

7.2.6 PMAO–UCNP Emission Spectra

The PMAO–UCNP powder was placed in a custom-designed sample holder and illuminated with a 978-nm laser coupled to a multimode fibre that was butted against the sample. The emitted signal was recorded in transmission by a calibrated spectrometer (Ocean Optics, USA) filtered with a short-pass emission filter, wavelength cut-off 842 nm (Semrock, USA).

7.2.7 PMAO–UCNP Absolute Conversion Efficiency (η_{uc}) Measurements

The η_{uc} measurements were performed in a calibrated integrating sphere setup as described previously [24, Chapter 6]. In short, an integrating sphere spatially integrates all radiant flux, thus absolute absorption and emission can be measured independent of scattering by the particles. The PMAO–UCNP in powder form was placed in a custom-made sample holder at one exit port of the integrating sphere and excited by 978-nm laser light delivered by a multimode optical fibre. Using appropriate filters and a photodiode placed at the perpendicular exit port of the sphere, both emitted power (P_{em}) and absorbed power (P_{abs}) were measured over a large range of excitation intensities. η_{uc} was calculated according to the definition, P_{em}/P_{abs} [W/W].

7.2.8 Cell Labelling

Human breast adenocarcinoma cells SK-BR-3 and Chinese hamster ovary cells CHO-K1 were purchased from American Type Culture Collection and cultured in RPMI 1640 medium (HyClone, USA) supplied with γ -glutamine and 10% fetal bovine serum (HyClone, USA). The cells were seeded on 8-well glass slides at a concentration of ca. 3×10^4 cells/ml. After 24-h cultivation at 37 °C in a CO₂-incubator (with 5% CO₂), the cells were inactivated by 1% formaldehyde to prevent nonspecific UCNP internalization. Nonspecific binding of the particles to the glass slide was also eliminated by incubating the sample with a blocking agent [1% bovine serum albumin (Bio-Rad, USA) in PBS] for 1 h. The Bn-scFv4D5 solution (in PBS with 0.1% bovine serum albumin and 0.1% Tween-20) was then applied for targeting Bn through the scFv4D5-HER2/neu interaction. After 1 h of the incubation, the cells were rinsed with PBS and treated with the UCNP-Bs (100 μ g/ml) colloid for 20 min. This time was considered to be sufficient to complete the formation of the UCNP-Bs:Bn-scFv4D5 complexes due to extremely high Bs:Bn affinity ($K_d \sim 10^{-14}$ M). Next, the cells were washed several times to remove unbound UCNP-Bs. Finally, the cells were fixed in 4% formaldehyde in PBS and mounted between a microscope slide and a coverslip. The negative control cell line was used to prove that the binding of UCNPs to the cancer cells was not a result of physical adsorption of the Bn-scFv4D5.

7.2.9 Laser-Illuminated Inverted Epi-Luminescence Microscopy

Laser (978 nm, LD980-01CW, CXCH-Photonics, China) excitation was delivered to the sample plane of a wide-field inverted epi-luminescence microscope (Olympus IX70, Japan) via a Köhler illumination scheme. An oil-immersion objective (100 \times , NA 1.30, Olympus, Japan) was used for bright-field cell imaging. A long-working distance dry objective (50 \times , NA 0.45, Olympus, Japan) was employed for UCNP-assisted imaging through the phantom layers to simulate an *in vivo* imaging procedure. The sample plane was imaged using an electron-multiplying CCD [EMCCD (iXon DU-885, Andor, Northern Ireland)] camera.

7.2.10 Phantom Fabrication

Melted agarose–water solution (1.5%) (Promega, Spain) was mixed with absorbing dyes [Magenta (Royal Talens, Holland) and black Indian ink (Winsor & Newton, UK)] and TiO₂ submicron particles [1 mg/ml (Sigma–Aldrich, Germany)] to model the scattering properties of breast tissue [25]. Uniformly thin and flat phantom layers were prepared by setting the warm agarose mixture between two glass plates spaced 0.4, 0.8, and 1.4 mm apart.

7.3 RESULTS AND DISCUSSION

7.3.1 Synthesis and Characterization of UCNP-Based Molecular Probe

We designed, synthesized, and characterized a new molecular probe for cancer cell imaging. This comprised a contrast agent — an UCNP coated with an amphiphilic polymer — and a targeting vector — a mini-antibody raised against HER2/neu receptors.

UCNP synthesis and surface functionalization

The UCNPs composed of $\text{NaYF}_4:\text{Yb,Er}$ were synthesized by performing a modified coordinate stabilization reaction. As-synthesized UCNPs were re-dispersed in *n*-hexane by sonication and then imaged by TEM. The results of TEM imaging showed particles 120 ± 20 nm in size and predominantly hexagonal in shape, as presented in Fig. 7.1(a), left panel. The hexagonal shape of the particles indicates the beta-phase of the host crystallite NaYF_4 , which is the most favourable for the energy transfer upconversion process [26]. The as-synthesized UCNPs coordinated with oleic acid hydrophobic moieties were surface-capped with PMAO [23]. Carboxylic groups of the PMAO that appeared as a result of the hydrolysis of anhydride functional groups became exposed outwards, producing hydrophilic UCNPs, i.e. stable in aqueous solutions. In addition, the hydrophilic terminals allowed covalent binding to biomolecules through the carboxylic groups. PMAO surface-capped nanoparticles were dispersed in water, sonicated, and imaged by TEM. As seen in Fig. 7.1(a), right panel, there was negligible change in the particle size during the surface capping procedure, as expected. The polymer coating is imaged as a supramolecular network of amphiphilic molecules juxtaposed on the core material and as thin layer fragments of low electron density (Fig. 7.1(a), right panel).

We also determined the mean hydrodynamic diameters of the PMAO-UCNP particles by means of dynamic light scattering (DLS), yielding 130 ± 20 nm (Fig. 7.1(b)), which corroborated the TEM size measurement, considering a $\pm 10\%$ size overestimation by DLS measurements). The produced aqueous colloid remained stable for at least 2 months, as confirmed by DLS measurements. The PMAO surface capping of UCNP altered its surface charge. Its zeta-potential was measured in water as -53 mV in comparison to that of -5 mV for the as-synthesized particles. The abundant surface carboxyl groups of the polymer layer were believed to build up this highly negative surface charge.

FTIR spectroscopy of the PMAO surface-capped particles further confirmed the successful surface modification of the UCNP sample. The results of the comparative analysis of PMAO-UCNP and pure PMAO are presented in Fig. 7.1(c). C–H stretching of CH_2 polymer groups at 2919 and 2851 cm^{-1} appeared in both UCNP and PMAO-UCNP samples. The maleic anhydride ring spectral signature is of particular note. It featured two peaks at 1858 and 1781 cm^{-1} in pure PMAO, which disappeared as a result of the hydrolysis upon the PMAO-UCNP transfer to water, with the corresponding anhydride ring opening and production of free carboxylic groups presented at 1734 and 1560 cm^{-1} [27,28]. The hydrolysis of a certain number of anhydride groups in pure PMAO is known to display an FTIR peak at 1710 cm^{-1} , which is present in Fig. 7.1(c) [28].

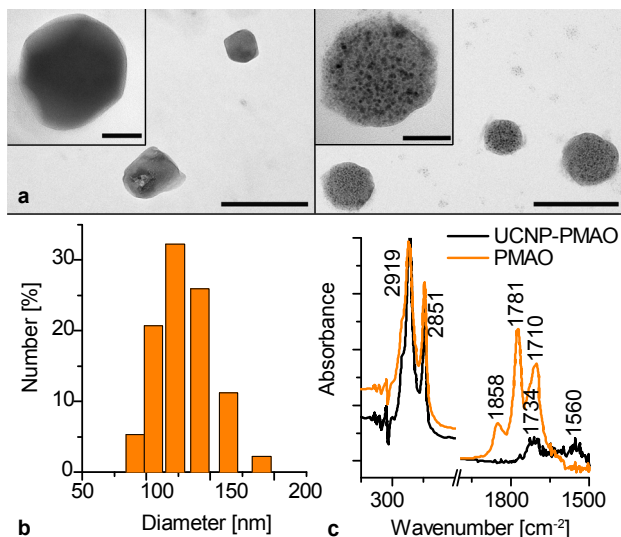


Fig. 7.1 | Characterization of upconversion nanoparticles surface-capped with amphiphilic polymer, PMAO. (a) Transmission electron microscopy imaging of as-synthesized (left panel) and PMAO-capped (right panel) UCNPs. Scale bar, 200 nm. Zoomed-in images of the UCNPs are shown in insets in the left top corners. Scale bar, 50 nm. Right panel, a PMAO polymer layer on an UCNP crystal is visualized as a granular structure that represents a supra-molecular network of amphiphilic molecules. (b) Histogram of the hydrodynamic size distribution of PMAO-UCNP obtained by dynamic light scattering measurements. This distribution remained unchanged for at least 2 months. (c) Fourier-transform infrared spectra of PMAO-UCNP and pure PMAO. The peak analysis points to the formation of the PMAO shell around the particles. See text for more details.

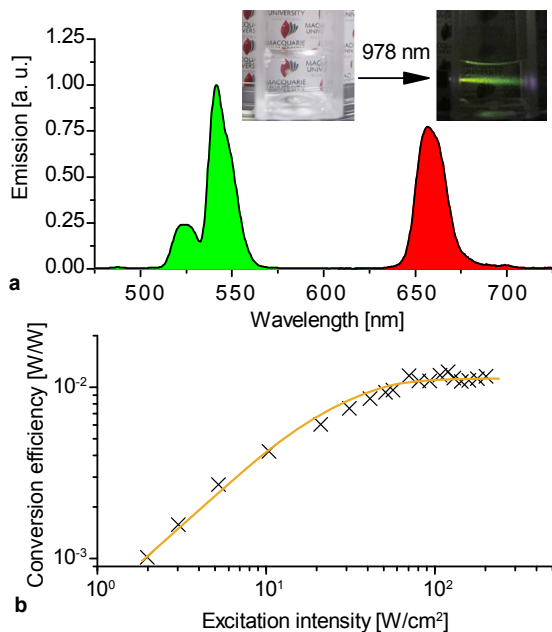


Fig. 7.2 | Photophysical characteristics of the PMAO-UCNP. (a) Emission spectrum of the PMAO-UCNP powder featuring three (unresolved) emission multiplets grouped in green and red wavelength regions. Inset, left panel, a cuvette with UCNP aqueous colloid exhibiting high transparency; right panel, green-colour emission along the 978-nm laser beam path captured under low ambient light condition. (b) Absolute conversion efficiency of PMAO-UCNP as a function of the excitation intensity at 978 nm, measured using a calibrated integrating sphere setup. The orange line is a guide to the eye, and saturation is reached at ~ 60 W/cm².

Photophysical properties of PMAO-UCNP

Optical characterization of the excitation and emission properties of UCNP and, in particular, PMAO-UCNP was performed. The choice of PMAO-UCNP was primarily dictated by its improved η_{uc} in comparison with the as-synthesized UCNP. Additionally, the PMAO-UCNP exhibited excellent immunity to environmental and surface conditions, so that its emission properties measured in powder form remained the same both in solution and after bioconjugation. The emission spectrum of PMAO-UCNP powder was acquired using a calibrated spectrometer with excitation by a 978-nm laser [excitation intensity (I_{ex}), 28 W/cm²], and is shown in Fig. 7.2(a). The spectrum featured three emission bands, which are known to result from the Er emission multiplets [11]. These multiplets can be grouped into two (green and red) wavelength bands, as respectively colour coded in Fig. 7.2(a). The optical absorption of the NIR excitation light at 978 nm and the η_{uc} of UCNP determine the intensity of the emitted signal. The η_{uc} is defined as the ratio of the emitted power to the absorbed power measured in W/W. The emitted power depends nonlinearly on the I_{ex} since each emitted photon is a result of the absorption of two or more photons followed by non-radiative relaxation processes. At high values of I_{ex} approaching saturation, η_{uc} reaches a plateau. Measurement of η_{uc} versus I_{ex} is essential for the evaluation of UCNP-assisted imaging performance. In Fig. 7.2(b), η_{uc} of PMAO-UCNP integrated over the entire emission spectrum is plotted versus I_{ex} . We note that the green-to-red emission ratio decreases as the I_{ex} is increased. η_{uc} of the PMAO-UCNP sample starts to saturate at $I_{ex} = 60$ W/cm² (I_{sat}) and reaches a maximum value of 1.2%. It is clear that the passivating surface coating affects η_{uc} and makes the coated UCNP much less susceptible to the environment and additional surface coating [29]. Hence, bioconjugation of PMAO-UCNP, as described in the next section, was of only minor influence to the η_{uc} of the polymer-coated UCNPs.

7.3.2 Design, Production and Target Delivery of UCNP-Bioconjugates

Bioconjugation

The PMAO-UCNP was grafted with mini-antibodies, scFv4D5, designed for targeted delivery to cancer cells that overexpress specific receptors HER2/neu. PMAO-UCNP and scFv4D5 were linked using a high-affinity molecular pair Bs:Bn.20,30 Bacterial ribonuclease Bn, and its inhibitor Bs, are small (12.4 and 10.2 kDa, respectively) proteins that are stable over a wide range of pH (from 2 to 12) and temperatures (50°C and 70°C, respectively), and have terminal groups accessible for covalent modifications and genetic fusion. A PMAO-UCNP bioconjugate was realized by its surface coating with Bs, thus forming the first submodule, while Bn was a part of the other submodule, which included an anti-HER2/neu scFv4D5 mini-antibody (Fig. 7.3(a) and 7.3(b)). The Bs-binding ability of the Bn-scFv4D5 was proved by measurement of the Bn ribonucleic activity inhibition by Bs (Fig. 7.4(a)) and the Bn-scFv4D5-HER2/neu affinity constant was calculated from Fig. 7.4(b) to be 1.62×10^9 M⁻¹ (Eqs. (7.1) and (7.2)). The PMAO-UCNP conjugation with Bs was implemented using a reaction with EDC and sulfo-NHS relying on the covalent linkage of the PMAO-UCNP carboxyl groups and Bs amino groups (Fig. 7.3(b)). The negatively charged Bs (pI 4.6) was favoured over the positively charged Bn (pI 8.9) for the conjugation reaction to avoid undesirable electrostatic adsorption due to the negative zeta-potential of the PMAO-UCNP [30].

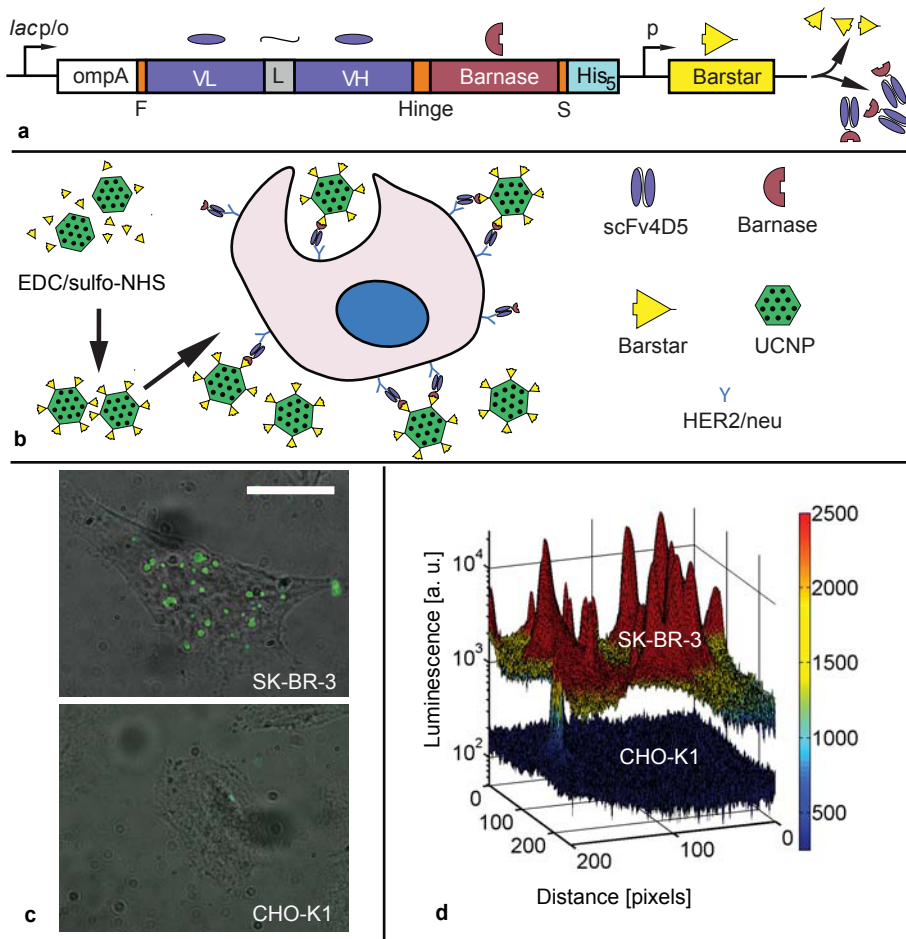


Fig. 7.3 | Cell labelling with UCNPs:Bs:scFv4D5 biocomplexes. (a) Targeting vector, Bs-scFv4D5 gene construction. The gene is under the control of a lac promoter (*lac p/o*) and the *ompA* signal peptide, and includes the N-terminal FLAG tag (F), VL-linker-VH oriented scFv4D5 mini-antibody, hinge linker (16 amino acids), Bs, short spacer S (Gly-Ala-Pro), and C-terminal His5-tag, localized sequentially. Bs coexpression is under the control of its own constitutive promoter (*p*) and required to suppress the Bs cytotoxicity. (b) The concept of cell labelling with self-assembled UCNP biocomplexes UCNPs:Bs:scFv4D5. (c) Epi-luminescence microscopy of the HER2/neu overexpressing SK-BR-3 cells labeled with UCNPs:Bs:scFv4D5. Scale bar, 20 μm . (d) Three-dimensional surface plot of the luminescence signal acquired from the CHO-K1 and SK-BR-3 cells incubated with UCNPs:Bs:scFv4D5. Although the labelled SK-BR-3 cells exhibited several discrete peaks due to UCNP biocomplex clusters, many more single and small clustered UCNP biocomplexes were also attached to these cells, resulting in higher overall signal level in between these peaks.

Specific Labelling of Cancer Cells with the UCNPs:Bs:scFv4D5 Complexes

Experimental confirmation of the bioconjugation reaction and the functionality of the UCNPs:Bs:scFv4D5 biocomplexes was performed by specific immobilization of these biocomplexes on cancer cells, more specifically, human breast adenocarcinoma cells SK-BR-3 known to overexpress HER2/neu, and fixed in 1% paraformaldehyde [31]. Chinese hamster ovary cells CHO-K1 devoid of HER2/neu were used as a negative control. Both cell lines were incubated with recombinant mini-antibody submodules Bs-scFv4D5 to bind to HER2/neu through the antibody-receptor interaction, so that Bs was immobilized on the

targeted cells. At the second incubation stage, UCNP-Bs was attached to the cell-immobilized Bn via high-affinity binding to Bs (Fig. 7.3(b)). Imaging of the UCNP biocomplex-treated cells using modified epi-luminescence microscopy under the 978-nm excitation showed that UCNP-Bs:BnscFv4D5 biocomplexes were immobilized on the SK-BR-3 cells with a 10-fold higher signal compared to the control CHO-K1 cells (Fig. 7.3(c)). The UCNP labelling level was estimated by image analysis of the luminescent signal integrated over the cell surface area using MATLAB software (Fig. 7.3(d)). The SK-BR-3 cells exhibited high overall UCNP labelling level with several discrete signals from UCNP clusters.

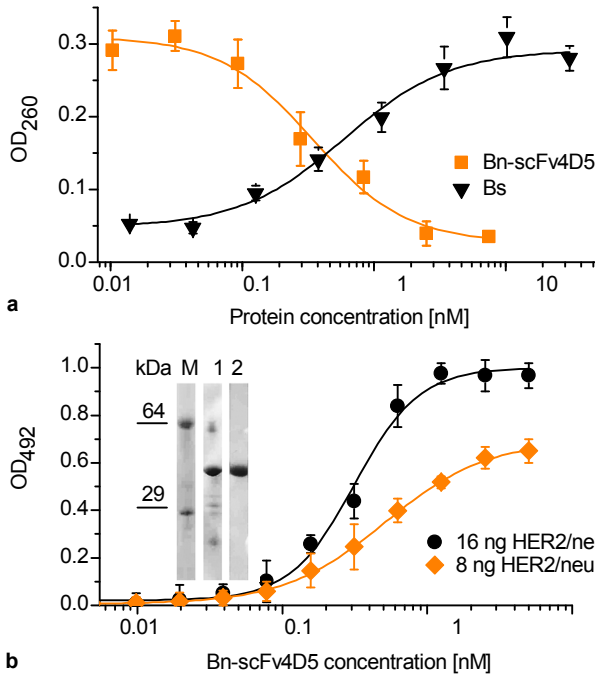


Fig. 7.4 | Functional characterization of the scFv4D5-Bn protein. (a) Assaying of Bn-scFv4D5 affinity to Bs through measurements of ribonucleic activity inhibition. (b) Determination of the Bn-scFv4D5 recombinant protein affinity to HER2/neu by enzyme-linked immunoassay ($K_{\text{off}} = 1.62 \times 10^9 \text{ M}^{-1}$). Inset, electrophoresis gel profile of the Bn-scFv4D5 after two steps of the purification procedure: M, protein marker; 1, Ni^{2+} affinity chromatography; and 2, ion-exchange chromatography

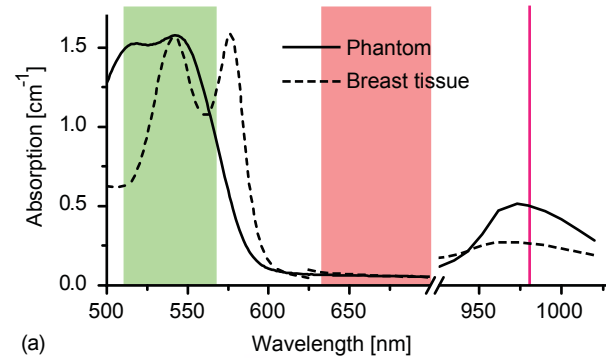
7.3.3 Evaluation of the Feasibility of UCNP-Assisted Optical Imaging in Human Breast Tissue

Breast tissue phantom

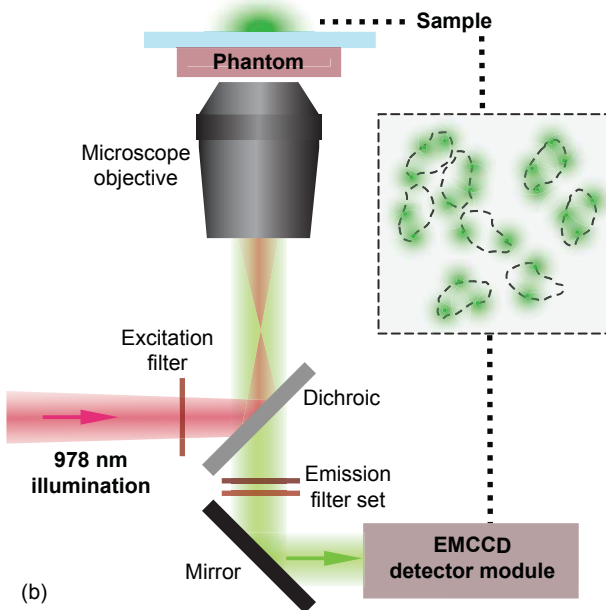
Since adenocarcinoma cells are hosted in human breast tissue, imaging contrast of these cells can be modelled experimentally, provided a human breast tissue model is available. To this end, we designed an agarose-based phantom that mimicked the optical absorption properties of live human breast tissue in the spectral ranges of the UCNP excitation and emission (Fig. 7.5(a)), and scattering in NIR region. The absorption of breast tissue was calculated, considering absorption of haemoglobin (0.002 mM) and oxy-haemoglobin (0.011 mM) in the green range and NIR light absorption of water [32]. The spectrum of breast tissue absorption in the red spectral range was obtained from *in vivo* measurements [33]. Agarose was chosen as the matrix, as its water content (about 99%) is commensurable with that of live breast tissue (10% to 60%), and resulted in slightly higher absorption of the excitation light compared to live tissue, i.e. by 0.2 cm^{-1} . The phantom and breast tissue absorption coefficients (μ_a) integrated over the relevant wavelength bands were similar

(green: $\mu_{a,breast} = 1.35 \text{ cm}^{-1}$, $\mu_{a,phantom} = 1.50 \text{ cm}^{-1}$, red: $\mu_{a,breast} = 0.06 \text{ cm}^{-1}$, $\mu_{a,phantom} = 0.06 \text{ cm}^{-1}$ and 978 nm: $\mu_{s,breast} = 0.3 \text{ cm}^{-1}$, $\mu_{s,phantom} = 0.5 \text{ cm}^{-1}$), see Fig. 7.5(a). The reduced scattering coefficient of breast tissue *in vivo* was simulated by adding TiO₂ submicron particles to the phantom [34]. The scattering coefficient and average cosine of scattering (g-value) in our phantom were defined by Mie calculations of 1 mg/ml TiO₂ particles in water. Matching the reduced scattering coefficient μ'_s (with $\mu'_s = (1-g)\mu_s$, μ_s being the scattering coefficient, and g is the anisotropy factor) at 978 nm recorded *in vivo* (978 nm: $\mu'_{s,breast} = 8$ to 12 cm^{-1} , $\mu'_{s,phantom} = 10 \text{ cm}^{-1}$) resulted in a decreased scattering coefficient of the phantom compared to live tissue for the green and red wavelength bands (red: $\mu'_{s,breast} = 13$ to 20 cm^{-1} , $\mu'_{s,phantom} = 6.9 \text{ cm}^{-1}$ and green: $\mu'_{s,breast} = 15$ to 22 cm^{-1} , $\mu'_{s,phantom} = 6.6 \text{ cm}^{-1}$) [33]. Matching μ'_s of live tissue and phantom material at 978 nm was crucial and hence prioritized in our modelling, since the scattering of 978-nm light primarily determined the luminescence signal decay with depth due to the nonlinear UCNP η_{uc} . As is seen from Fig. 7.5(a), UCNP excitation at 980 nm is suboptimal for bioimaging due to the onset of the water absorption, and the use of the excitation at 915 nm is sometimes

preferable, although the excitation efficiency is lower. The use of a commercially available 915-nm semiconductor laser as an excitation source for an UCNP luminescence can considerably increase the imaging depth as was reported by Zhan et al. [18].



(a)



(b)

Fig. 7.5 | Experimental modelling of UCNP-assisted optical imaging. (a) Optical absorption spectrum of the tissue simulating phantom designed to reproduce the key optical properties of breast tissue in the UCNP excitation and emission spectral ranges (solid line). The tissue absorption spectrum (dashed line) is obtained from the literature. The UCNP emission in green and red bands and excitation in the NIR region are shown as shaded areas. (b) Schematic diagram of the optical imaging setup; UCNP-labelled cancer cells are imaged through the phantom mimicking absorption and scattering properties of breast tissue.

Experimental modelling of UCNP-assisted cancerous lesion imaging

An optical phantom simulating breast tissue optical properties provides an excellent model to assess the prospects of *in vivo* UCNP-targeted imaging of breast cancer lesions. The cancer cells labelled with UCNP-Bs:Bn-scFv4D5 biocomplexes were covered with a stack of phantom layers (0.4 to 2.0 mm) and imaged using a modified epi-luminescence microscope, see Fig. 7.5(b). A long-working distance objective lens allowed stacking thin phantom layers on top of the sample, while re-adjusting the objective lens distance to the sample. The signal-to-noise ratio (SNR) was defined as a ratio of the luminescence signal to the standard deviation of the signal, where the signal was estimated as a sum of the pixel values over the sample area with the background subtracted. The sample area was a cellular region outlined as inferred from the bright-field microscopy (Fig. 7.5(b), dashed lines). The background level was estimated as the mean pixel value outside the illumination spot in the same image. The total noise level (N_{total}) was defined as:

$$N_{total} = \sqrt{N_{shot}^2 + N_{dark}^2 + N_{read}^2 + N_{rest}^2} \quad (7.3)$$

where N_{shot} , N_{dark} , N_{read} and N_{rest} are signal shot noise multiplied by the EM-characteristic multiplicative noise factor 1.4, dark noise, read noise, and rest noise, respectively, all measured in number of electrons [e^-] [35,36]. For the experimental image data, the dark, read, and rest noises were estimated as the standard deviation of the dark background. The signal shot noise was derived from the acquired upconversion signal (*signal*):

$$N_{shot} = \sqrt{signal} \quad (7.4)$$

The SNR of the same sample area is plotted versus phantom thickness in Fig. 7.6. According to the SNR estimation and observed image contrast, the signals from the UCNP-labelled SK-BR-3 cells were clearly observable through the phantom up to 1.6-mm thick (SNR = 4.5, Fig. 7.6).

We note that the excitation intensity at 978 nm, I_{ex} , decreases with the phantom thickness, and at a depth greater than 0.4 mm it is below I_{sat} as found using the Lambert–Beer law:

$$P(z) = P(0)e^{-\mu_{tr}z} \quad (7.5)$$

where μ_{tr} is the transport attenuation coefficient (mm^{-1}) defined as a sum of the absorption, μ_a and reduced scattering coefficients μ'_s [24]. The decrease in I_{ex} below I_{sat} yields lower η_{uc} that contributes to SNR loss, in addition to increased attenuation of the emitted light with the phantom thickness.

Quantitative imaging of the UCNP-labelled SK-BR-3 cells allowed estimation of the total number of UCNP biocomplexes per cell, using the following equation:

$$S_{UCNP} = N_{UCNP} N_{YB} \sigma_{abs,YB} I_{ex} \eta_{UC} \zeta_{total} \quad (7.6)$$

where S_{UCNP} is the detected luminescent signal (counts/s); N_{UCNP} is the number of UCNP biocomplexes per cell; N_{Yb} is the total number of Yb ions per UCNP crystal; $\sigma_{abs,Yb}$ is the Yb absorption cross section ($1 \times 10^{-20} \text{ cm}^2$); I_{ex} (W/cm^2); η_{uc} according to Fig. 7.2(b); and ζ_{total} (counts/W/s) is the spectral calibration coefficient of the detection path in the microscope system calculated as described in Chapter 6 [24], Eq. 6.2.

The total number of UCNP biocomplexes per SK-BR-3 cell *in vitro* was calculated to be $[2.8 \pm 0.5] \times 10^4$ using Eq. (7.6). In order to put this estimation in the context of an *in vivo* imaging scenario, we made use of the cross-comparison between the *in vivo* and *in vitro* labelling efficiency reported to be ca. 10-fold less for the *in vivo* case [37,38]. Therefore, the number of UCNPs in one breast cancer cell *in vivo* was estimated to be ~ 3000 .

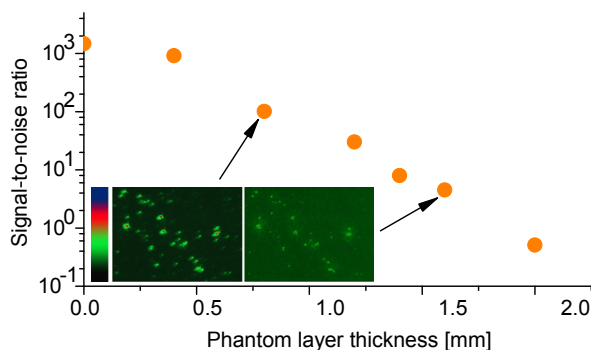


Fig. 7.6 | UCNP-labelled SK-BR-3 cell imaging through a breast tissue simulating phantom at excitation intensity $100 \text{ W}/\text{cm}^2$. The signal-to-noise ratio was estimated as the total signal from one SK-BR-3 cell divided by the total noise (see text for details), and plotted versus the phantom thickness. Inset shows a false colour image of the UCNP-labelled SK-BR-3 cells through 0.8 and 1.6-mm phantom layers, arrows point to the corresponding data points in the graph; left panel, colour bar.

Theoretical modelling of *in vivo* imaging

The experimental data of the UCNP-assisted imaging sets the framework for the estimation of limits of *in vivo* detection of UCNP-labelled breast cancer lesions versus depth in breast tissue. Equation (7.5) was used to calculate the attenuation of the excitation and emission power, P at depth z due to absorption and scattering in tissue. This power relationship holds for both the excitation light travelling into the tissue toward the UCNP sample and the emitted light travelling backward.

Initially, we calculated the UCNP signal versus the phantom thickness and compared it with that acquired experimentally (cf. Fig. 7.6). The experimental data were obtained by adding up all pixels from the area occupied by the SK-BR-3 cells, subtracting the background, and normalizing for the EM gain, exposure time, microscope throughput, and camera sensitivity. The UCNP signal *in vitro* for one SK-BR-3 cell versus the phantom thickness is shown in Fig. 7.7 plotted as separate data points (triangles). The UCNP signal *in vitro* was also modelled using Eqs. (7.5) and (7.6), with the optical properties of the phantom and $I_{ex} = 100 \text{ W}/\text{cm}^2$ as parameters. As is shown in Fig. 7.7 (orange solid line), the modelled signal dependency on phantom thickness fits the data points very well for the entire depth range down to 2 mm. Therefore, extrapolation of the signal to the greater depths pertinent for

in vivo optical imaging is feasible. The UCNP-assisted imaging limit was theoretically estimated considering early-stage cancer tumour diagnostics under the maximum permissible laser exposure condition. A total number of ~ 160 breast cancer cells localized in the imaging volume $\sim 260 \times 260 \times 10 \mu\text{m}^3$ were estimated, considering the EMCCD sensor optically conjugated with the imaging plane via a $50\times$ objective lens. A pulse energy of 0.7 J/cm^2 ($I_{\text{ex}} = 710 \text{ W/cm}^2$) of the excitation beam for a 1 ms pulse duration was calculated as the maximum permissible exposure for skin [39]. The camera acquisition parameters were exposure time 1 ms and EM gain $300\times$. We assumed an optimized imaging system with the background completely suppressed [14]. The calculated UCNP signal intensity versus depth in tissue is shown in Fig. 7.7 (black solid line). As can be seen, the modelled *in*

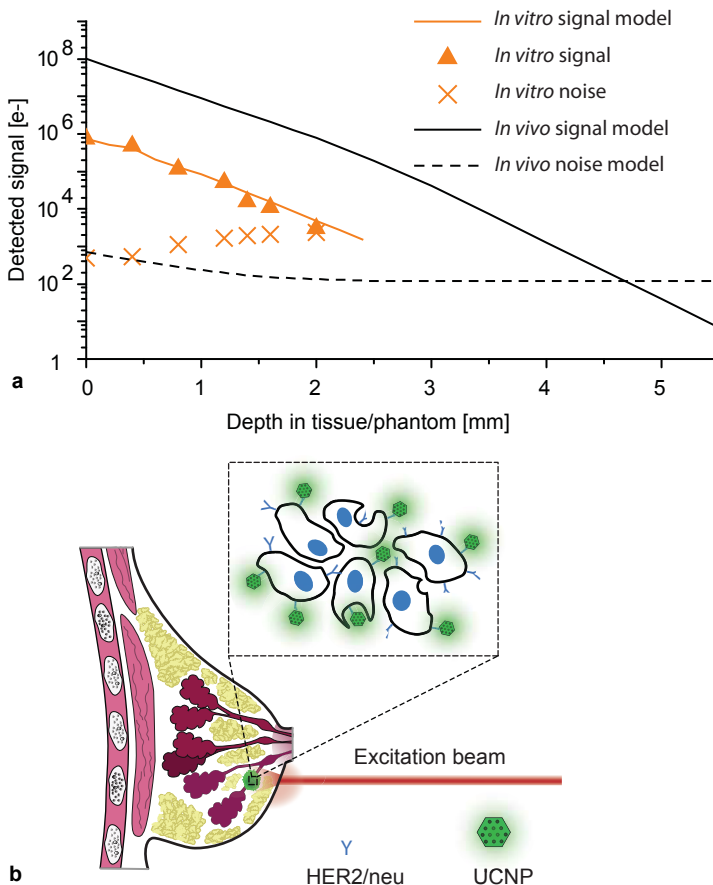


Fig. 7.7 | Theoretical estimation of UCNP-assisted *in vivo* optical imaging sensitivity: signal intensity and noise level versus the depth in tissue. **(a)** The theoretically modelled UCNP signal *in vitro* from one cell (orange solid line) is plotted as a function of the phantom thickness, which fits the experimental SK-BR-3 cell imaging data (triangles). *In vivo* UCNP signal (—, black solid line), *in vitro* (×, orange crosses) and *in vivo* (---, black dashed line) noise levels are plotted versus depth in tissue/phantom. ~ 160 (SK-BR-3) breast cancer cells localized within an imaging volume of $\sim 260 \times 260 \times 10 \mu\text{m}^3$ were modelled, considering ~ 3000 UCNP-Bs: Bn-scFv4D5 biocomplexes immobilized on each cell by HER2/neu, as schematically drawn in **(b)**.

vivo signal of a tumour cluster is higher than that of the experimental *in vitro* signal. This is attributed to the higher number of cells in the sample volume, normalized to the reduced scattering coefficient in the green and red regions and the increased I_{ex} , even though the lower labelling efficiency was taken into account (Eqs. (7.5) and (7.6)). The slope change of this curve at ca. 2 mm is explained by noting that I_{ex} is above the saturation intensity level within 2 mm from the surface in tissue yielding a nearly constant η_{uc} (see Fig. 7.2(b)). As the depth increases, I_{ex} and consequently η_{uc} decrease, thus contributing to the negative slope. The standard deviation of the signal was estimated to be less than 20%, with the main components due to the labelling variation from cell to cell, and noise. The UCNP-signal can be reliably measured only when it is well above the noise level. The *in vitro* noise was estimated as described above, and plotted in Fig. 7.7 as data points (\times). The relatively high noise level due to the excitation light at 978 nm bleeding through the filters can be completely suppressed, e.g. by employing time-gated detection [14] as plotted in Fig. 7.7 (black dashed line), where the dark and read noise were specified by the manufacturer, and the rest noise was zero. As one can see, the UCNP signal approaches the noise level beyond 4-mm depth in tissue, which represents a significant range for a number of applications, including early-stage breast cancer tumour diagnostics and image-guided surgery [4].

7.4 CONCLUSION

Optical imaging of an early-stage human breast cancer lesion labelled with luminescent UCNPs was modelled using cell cultures and optical phantoms. Human breast adenocarcinoma cells SK-BR-3 that overexpress epidermal growth factor receptor HER2/neu were targeted by polymer-capped UCNPs grafted with an anti-HER2/neu targeting vector via a high-affinity molecular pair Bs:Bn. Selective binding of the UCNP-Bs:Bn-scFv4D5 biocomplexes to the SK-BR-3 cells (the ratio 10:1 as compared to a negative control) was demonstrated. The luminescence signal of the UCNPs was detectable even through a 1.6-mm thick agarose phantom mimicking breast tissue optical properties. A theoretical model based on the experimental data predicted the feasibility of *in vivo* optical imaging at a depth of up to 4 mm in live breast tissue, under the reasonable assumption of complete suppression of background signals due to excitation light scattering and biological tissue autofluorescence, which is feasible given the UCNP luminescence properties. We believe this study demonstrates considerable potential for UCNP-assisted optical imaging for early-stage cancer diagnostic and image-guided surgery applications.

7.5 ACKNOWLEDGMENTS

We would like to thank Dr. A.N. Bykov for stimulating discussion on the theoretical aspects of modelling biological tissue phantoms. We wish to acknowledge support of the Russian Foundation of Basic Research, Grant Nos. 11-04-12113, 12-04- 01258-a, and 13-02-01138.

7.6 REFERENCES

1. H. Soliman et al., "Functional imaging using diffuse optical spectroscopy of neoadjuvant chemotherapy response in women with locally advanced breast cancer," *Clin. Cancer Res.* 16(9), 2605–2614 (2010).
2. L. V. Wang, "Multiscale photoacoustic microscopy and computed tomography," *Nat. Photonics* 3(9), 503–509 (2009).
3. R. Weissleder, "A clearer vision for *in vivo* imaging," *Nat. Biotechnol.* 19(4), 316–317 (2001).
4. S. Achilefu, "Lighting up tumors with receptor-specific optical molecular probes," *Technol. Cancer Res. Treat.* 3(4), 393–409 (2004).
5. Y. Ye et al., "Design, synthesis, and evaluation of near infrared fluorescent multimeric RGD peptides for targeting tumors," *J. Med. Chem.* 49(7), 2268–2275 (2006).
6. T. A. Zdobnova et al., "Fluorescent immunolabeling of cancer cells by quantum dots and antibody scFv fragment," *J. Biomed. Opt.* 14(2), 021004 (2009).
7. S. M. Deyev and E. N. Lebedenko, "Multivalency: the hallmark of antibodies used for optimization of tumor targeting by design," *Bioessays* 30(9), 904–918 (2008).
8. F. Leblond et al., "Pre-clinical whole-body fluorescence imaging: review of instruments, methods and applications," *J. Photochem. Photobiol. B* 98(1), 77–94 (2010).
9. N. M. Idris et al., "Tracking transplanted cells in live animal using upconversion fluorescent nanoparticles," *Biomaterials* 30(28), 5104–5113 (2009).
10. T. W. Prow et al., "Quantum dot penetration into viable human skin," *Nanotoxicology* 6(2), 173–185 (2012).
11. H. X. Mai et al., "Highly efficient multicolor upconversion emissions and their mechanisms of monodisperse NaYF₄:Yb, Er core and core/shell-structured nanocrystals," *J. Phys. Chem. C* 111(37), 13721–13729 (2007).
12. R. H. Page et al., "Upconversion-pumped luminescence efficiency of rare-earth-doped hosts sensitized with trivalent ytterbium," *J. Opt. Soc. Am. B* 15(3), 996–1008 (1998).
13. C. Vinegoni et al., "Transillumination fluorescence imaging in mice using biocompatible upconverting nanoparticles," *Opt. Lett.* 34(17), 2566–2568 (2009).
14. K. Hanaoka et al., "Time-resolved long-lived luminescence imaging method employing luminescent lanthanide probes with a new microscopy system," *J. Am. Chem. Soc.* 129(44), 13502–13509 (2007).
15. T. Cao et al., "High-quality water-soluble and surface-functionalized upconversion nanocrystals as luminescent probes for bioimaging," *Biomaterials* 32(11), 2959–2968 (2011).
16. Q. Liu et al., "Sub-10 nm hexagonal lanthanide-doped NaLuF₄ upconversion nanocrystals for sensitive bioimaging *in vivo*," *J. Am. Chem. Soc.* 133(43), 17122–17125 (2011).
17. L. Xiong et al., "High contrast upconversion luminescence targeted imaging *in vivo* using peptide-labeled nanophosphors," *Anal. Chem.* 81(21), 8687–8694 (2009).
18. Q. Q. Zhan et al., "Using 915-nm laser excited Tm³⁺/Er³⁺/Ho³⁺ doped NaYbF₄ upconversion nanoparticles for *in vitro* and deeper *in vivo* bioimaging without overheating irradiation," *ACS Nano* 5(5), 3744–3757 (2011).
19. C. Wang, L. Cheng, and Z. Liu, "Research spotlight: upconversion nanoparticles for potential cancer theranostics," *Ther. Delivery* 2(10), 1235–1239 (2011).
20. S. M. Deyev et al., "Design of multivalent complexes using the barnase-barstar module," *Nat. Biotechnol.* 21(12), 1486–1492 (2003).
21. G. W. Rushizky et al., "Studies on B. subtilis ribonuclease. I. Characterization of enzymatic specificity," *Biochemistry* 2(4), 787–793 (1963).
22. J. D. Beatty, B. G. Beatty, and W. G. Vlahos, "Measurement of monoclonal antibody affinity by non-competitive enzyme immunoassay," *J. Immunol. Methods* 100(1–2), 173–179 (1987).
23. T. Pellegrino et al., "Hydrophobic nanocrystals coated with an amphiphilic polymer shell: a general route to water soluble nanocrystals," *Nano Lett.* 4(4), 703–707 (2004).
24. A. Nadort et al., "Quantitative imaging of single upconversion nanoparticles in biological tissue," *PLoS One* 8(5), e63292 (2013).
25. A. V. Bykov et al., "Skin phantoms with realistic vessel structure for OCT measurements," *Proc. SPIE* 7376, 73760F (2010).
26. F. Wang et al., "Synthesis of polyethylenimine/NaYF₄ nanoparticles with upconversion fluorescence," *Nanotechnology* 17(23), 5786–5791 (2006).
27. L. S. Li et al., "Studies of nanoparticulate cadmium sulfide in amphiphilic polymaleic acid octadecanol ester Langmuir–Blodgett films," *Supramol. Sci.* 5(5–6), 475–478 (1998).

28. S. Song, L. Liu, and J. Zhang, "Annealing improves tribological property of poly (octadecene-alt-maleic anhydride) self-assembled film," *Appl. Surf. Sci.* 257(23), 10254–10260 (2011).
29. G. S. Yi and G. M. Chow, "Water-soluble NaYF₄:Yb; Er (Tm)/NaYF₄/ polymer core/shell/shell nanoparticles with significant enhancement of upconversion fluorescence," *Chem. Mater.* 19(3), 341–343 (2007).
30. V. K. A. Sreenivasan et al., "Barstar:barnase—a versatile platform for colloidal diamond bioconjugation," *J. Mater. Chem.* 21(1), 65–68 (2011).
31. N. E. Hynes et al., "Overexpression of the c-erbB-2 protein in human breast tumor cell lines," *J. Cell. Biochem.* 39(2), 167–173 (1989).
32. H. Heusmann, J. G. Koelzer, and G. Mitic, "Characterization of female breasts *in vivo* by time-resolved and spectroscopic measurements in the near infrared spectroscopy," *J. Biomed. Opt.* 1(4), 425–434 (1996).
33. A. Pifferi et al., "Spectroscopic time-resolved diffuse reflectance and transmittance measurements of the female breast at different inter-fiber distances," *J. Biomed. Opt.* 9(6), 1143–1151 (2004).
34. A. V. Bykov et al., "Multilayer tissue phantoms with embedded capillary system for OCT and DOCT imaging," *Proc. SPIE* 8091, 80911R (2011).
35. M. S. Robbins and B. J. Hadwen, "The noise performance of electron multiplying charge-coupled devices," *IEEE Trans. Electron. Devices* 50(5), 1227–1232 (2003).
36. J. C. Waters, "Accuracy and precision in quantitative fluorescence microscopy," *J. Cell Biol.* 185(7), 1135–1148 (2009).
37. S. R. Benhabbour et al., " *In vitro* and *in vivo* assessment of targeting lipid-based nanoparticles to the epidermal growth factor-receptor (EGFR) using a novel heptameric ZEGFR domain," *J. Controlled Release* 158(1), 63–71 (2011).
38. J. A. Khan et al., "Designing nanoconjugates to effectively target pancreatic cancer cells *in vitro* and *in vivo*," *PLoS One* 6(6), e20347 (2011).
39. Standards Australia/Standards New Zealand, AS/NZS 60825, pp. 1–48, SAI Global Limited, Sydney, AU and Wellington, NZ (2012).